Evaluation of welding damage in welded tubular steel structures using guided waves and a probability-based imaging approach

2011 Smart Mater. Struct. 20 015018

(http://iopscience.iop.org/0964-1726/20/1/015018)

Smart Mater. Struct. **20** (2011) 015018 (15pp) doi:10.1088/0964-1726/20/1/015018

Evaluation of welding damage in welded tubular steel structures using guided waves and a probability-based imaging approach

Xi Lu[1,2], Mingyu Lu[2], Li-Min Zhou[2,4], Zhongqing Su[2], Li Cheng[2], Lin Ye[2,3] and Guang Meng[1]

[1] State Key Laboratory of Mechanical System and Vibration, Shanghai Jiao Tong University, Shanghai 200240, People's Republic of China
[2] Department of Mechanical Engineering, The Hong Kong Polytechnic University, Kowloon, Hong Kong SAR
[3] Laboratory of Smart Materials and Structures (LSMS), Centre for Advanced Materials Technology (CAMT), School of Aerospace, Mechanical and Mechatronics Engineering, The University of Sydney, NSW 2006, Australia

E-mail: MMLMZHOU@inet.polyu.edu.hk

Received 21 January 2010, in final form 4 October 2010
Published 23 December 2010
Online at stacks.iop.org/SMS/20/015018

Abstract
Welded tubular steel structures (WTSSs) are widely used in various engineering sectors, serving as major frameworks for many mechanical systems. There has been increasing awareness of introducing effective damage identification and up-to-the-minute health surveillance to WTSSs, so as to enhance structural reliability and integrity. In this study, propagation of guided waves (GWs) in a WTSS of rectangular cross-section, a true-scale model of a train bogie frame segment, was investigated using the finite element method (FEM) and experimental analysis with the purpose of evaluating welding damage in the WTSS. An active piezoelectric sensor network was designed and surface-bonded on the WTSS, to activate and collect GWs. Characteristics of GWs at different excitation frequencies were explored. A signal feature, termed 'time of maximal difference' (ToMD) in this study, was extracted from captured GW signals, based on which a concept, *damage presence probability* (DPP), was established. With ToMD and DPP, a probability-based damage imaging approach was developed. To enhance robustness of the approach to measurement noise and uncertainties, a two-level image fusion scheme was further proposed. As validation, the approach was employed to predict presence and location of slot-like damage in the welding zone of a WTSS. Identification results have demonstrated the effectiveness of the developed approach for identifying damage in WTSSs and its large potential for real-time health monitoring of WTSSs.

(Some figures in this article are in colour only in the electronic version)

1. Introduction

Large-scale engineering structures and assets, e.g., power plants, bridges, pipelines and transportation vehicles, are becoming ubiquitous. However, their failure during operation, as a consequence of the occurrence of structural damage in critical components such as the wheel or bogie system of a train carriage, can result in immense life and monetary loss. For example, the German Eschede train crash in 1998, the world's most serious high-speed train disaster, leading to 200 casualties, was attributed to cracks in the wheel rims under repetitive loads (500 000/day) [1]. In 2006 a

[4] Author to whom any correspondence should be addressed.

number of cracks detected in the bogie systems of Hong Kong Mass Transit Railway (MTR) trains, made of welded metallic tubular structures, awakened momentous public attention. 'The excessive vibration experienced by the trains and material fatigue crack was the dominant reason', MTR proclaimed [2]. In the rail industry, train carriages approaching their designed service life are not exceptional, entering the senior age of a train carriage. The older these trains become the more critical defects they may have. These defects can progressively deteriorate as structures get old and undergo fatigue loads. There is no doubt that failure of these public transportation vehicles during their operation can lead to irretrievable and catastrophic consequences.

With safety being the paramount factor in any industry, especially public transportation, dependability and durability criteria must be strictly met, entailing the rapid development of nondestructive evaluation (NDE) techniques. Though playing a significant role in preventing failure from happening, most of today's NDE techniques in industry (visual inspection, radioscopy, ultrasonics, laser interferometry, thermography, eddy-current, electromagnetic inspection, etc [3–7]) are conducted at a periodical interval, regardless of the working condition changes and progressive deterioration of structures (i.e., non-condition-based). They cost a lot but deliver relatively poor efficiency. For example, ultrasonic inspection, the most widely adopted NDE approach in the railway industry, is operated at a very slow speed, consuming much time to scan whole train structures. To ensure the functionality of ultrasonic probes, downtime of the structure is often required. Moreover, these techniques often neglect tiny damage until it grows to a conspicuous level.

With recognition of the above-mentioned inefficiency, a condition-based philosophy in conjunction with embedded active sensor networks has been established since the 1990s to revamp the traditional NDE [8–12] and provide a continuous and automated surveillance on structural health status by considering the condition updates and structural ageing. This technology is termed structural health monitoring (SHM) [13]. Embedding active sensor networks in critical sections of train structures is a promising solution, in which multi-functional sensors are capable of sensing and providing continuous information on structural integrity status, facilitating awareness of defects at an early stage. It has been demonstrated that an effective SHM technique can reduce the total maintenance cost of an engineering system by over 30% [14], accompanied by a substantial improvement of reliability and safety. Amongst various SHM tools, guided waves (GWs) are particularly promising for their superb capabilities including low attenuation, strong penetration, fast propagation, omnidirectional dissemination, convenience of activation and acquisition, low energy consumption and, most importantly, high sensitivity to structural damage even when it is small in size [11]. GW-based damage identification and SHM techniques have been practised in a large number of applications, including those of crack(s) identification in metallic/composite plates [15–20], thermal protection systems [21], bridge/aircraft components [22, 23] and cylindrical pipes [24], with demonstrated effectiveness. In particular, instantaneous baseline measurement and RAPID (reconstruction algorithm for probabilistic inspection of defects) were reported by Anton *et al* [15] and Zhao *et al* [23], respectively, and these novel algorithms and experiences contributed much to the development of the recommended approach in this paper.

Research on damage identification and SHM in real train/rail structures has been addressed by different research groups [25–27]. However, limited activities have been directed to the development of GW-based techniques for train structures. In comparison with plate-like structures such as those widely used in the aerospace industry, welded tubular steel structures (WTSSs) are often seen in train structures, serving as the framework of the bogie system of a train carriage. A WTSS is very thick and large in size, necessitating a higher magnitude of wave excitation to cover a reasonable area. Multiple wave modes in the tubular structures and their interactions with damage and complex boundaries present substantial obstacles for effective signal interpretation. Moreover, demanding working conditions cause complex boundary conditions, contributing to additional difficulties in practical application.

Motivated by the above-addressed deficiencies in today's SHM for train structures, a GW-based damage identification approach has been specialized for the WTSS used in the bogie system of a train carriage. Both FEM and experimental analysis were employed to investigate the propagation of GWs in a WTSS of rectangular cross-section with welding damage, i.e., a true-scale model of a train bogie frame segment. With the assistance of an active piezoelectric sensor network, GW signals were activated and captured, from which a signal feature, termed 'time of maximal difference' (ToMD), was extracted to establish *damage presence probability* (DPP). The continuous wavelet transform (CWT) and Hilbert transform (HT) are employed to implement signal purification and feature highlighting. A probability-based damage imaging approach was developed based on ToMD. As validation, the approach was used to predict presence and location of slot-like damage in the welding zone of a WTSS. Furthermore, a two-level image fusion scheme using different strategies was developed to enhance the tolerance of the approach to signal noise.

2. Propagation characteristics of GWs in WTSS with welding damage

2.1. Description of the problem

A bogie frame dismantled from a real train carriage is shown in figure 1(a), which is comprised of a number of WTSSs of rectangular cross-sections. The WTSS in a train carriage is a grillage-like structure designed to carry various operational loads. The complexity in geometry of a WTSS and numerous attachments make the access to critical areas where structural damage is likely to exist highly prohibitive, posting a great challenge in implementing damage identification and SHM techniques based on GWs. With the occurrence of damage, the propagation characteristics of GWs in a WTSS become

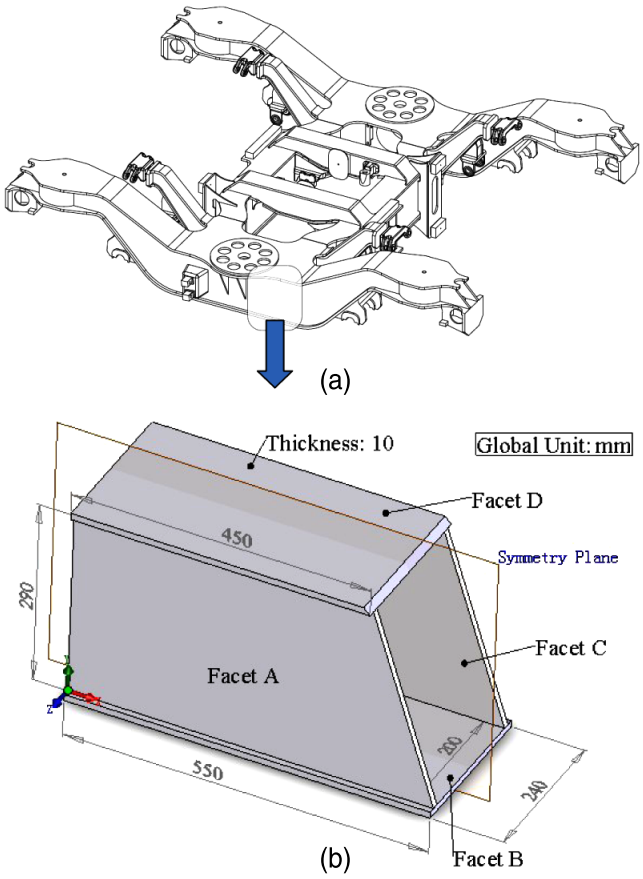

Figure 1. (a) A typical bogie frame of a train carriage consisting of a number of WTSSs and attachments; and (b) geometrical details of the WTSS under investigation.

Table 1. Material properties of the WTSS.

Density	7.85 g cm^{-3}
Poisson's ratio	0.28
Elastic constant, E	210 GPa

more difficult to interpret. To investigate the propagation of GWs in WTSSs, a WTSS, a true-scale section model of the bogie frame from an HK MTR train carriage, was fabricated, as shown schematically in figure 1(b). The WTSS consists of four facets which are pre-welded to shape a tube of rectangular cross-section. The detailed geometrical dimensions are shown in the same figure and the material properties of the WTSS are detailed in table 1. Considering most damage in the WTSS initiates and propagates from welding zones between adjacent facets, slot-like damage in the welding zone between Facets A and B was focused on. As envisaged, material inhomogeneity and uneven thermal treatment during welding might potentially impact on propagation characteristics of waves in WTSSs. For the development of the approach, the discussed WTSS was hypothesized as homogeneous and thermally treated well and evenly.

An active sensor network consisting of twelve circular piezoelectric lead zirconate titanate (PZT) wafers, 6.9 mm in diameter and 0.5 mm in thickness each, was symmetrically surface-mounted to Facets A and C. Each PZT wafer can

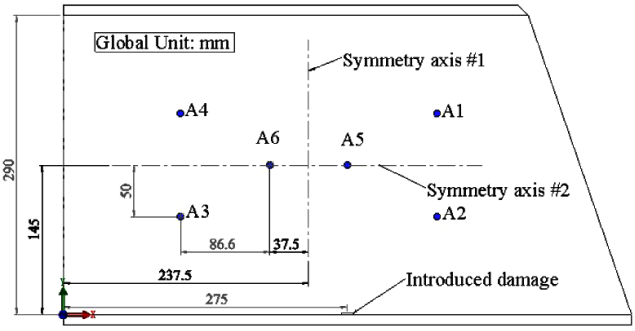

Figure 2. Layout of the active PZT sensor network surface-bonded to the WTSS (diagram showing half of the sensor network on Facet A, and Facet C sharing the same network configuration).

function as either the actuator to generate waves or sensor to receive damage-scattered waves in accordance with the dual piezoelectric effects. The detailed layout and nomenclature of PZT wafers on Facet A are shown in figure 2. A simulated damage scenario, a through-thickness slot-like welding defect, 12 mm long, 1 mm wide and 10 mm deep, was assumed in the welding zone between Facets A and B (x-axis), with its centre (i.e. 'damage centre' hereafter) being 275 mm away from the origin of the coordinate system in figure 2. The simulated damage was at a macroscopic level, much greater than the realistic damage in real engineering structures. However, for the development of the approach, the damage was simulated to capture pronounced wave scattering. In the active sensor network, to minimize the influence of complex boundary reflections from the opposite facet upon wave signal interpretation, each sensor was limited to capturing GW signals activated by actuators located on the same facet. Therefore, the displayed sensor network segment on Facet A (half of the entire sensor network) is able to render thirty sensing paths, consisting of one actuator and one sensor each. For convenience of discussion each sensing path is denoted by A_mA_n for those on Facet A or C_mC_n for those on Facet C ($m, n = 1, 2, \ldots, 6$, but $m \neq n$) in what follows.

Various GW modes co-exist depending on the geometric features and excitation frequencies, which can be deemed as the superposition of a series of longitudinal and transverse modes [28]. Generally speaking, both the longitudinal and transverse modes are sensitive to structural damage and both can be used for identifying damage, but the former is used more frequently. Recently, there has been increasing awareness of using the transverse mode for damage identification [9, 22]. Its merits, in comparison with the longitudinal mode, include: (i) shorter wavelength at a given excitation frequency (in recognition of the fact that the half wavelength of a selected wave mode must be shorter than or equal to the damage size to allow the wave to interact with the damage); and (ii) larger signal magnitude (the transverse mode in a wave signal is usually much stronger than the longitudinal mode if two modes are activated simultaneously, giving a signal with high signal-to-noise ratio (SNR), though it attenuates more quickly). In this study, attention was focused on the transverse mode which dominated the sensed wave signals.

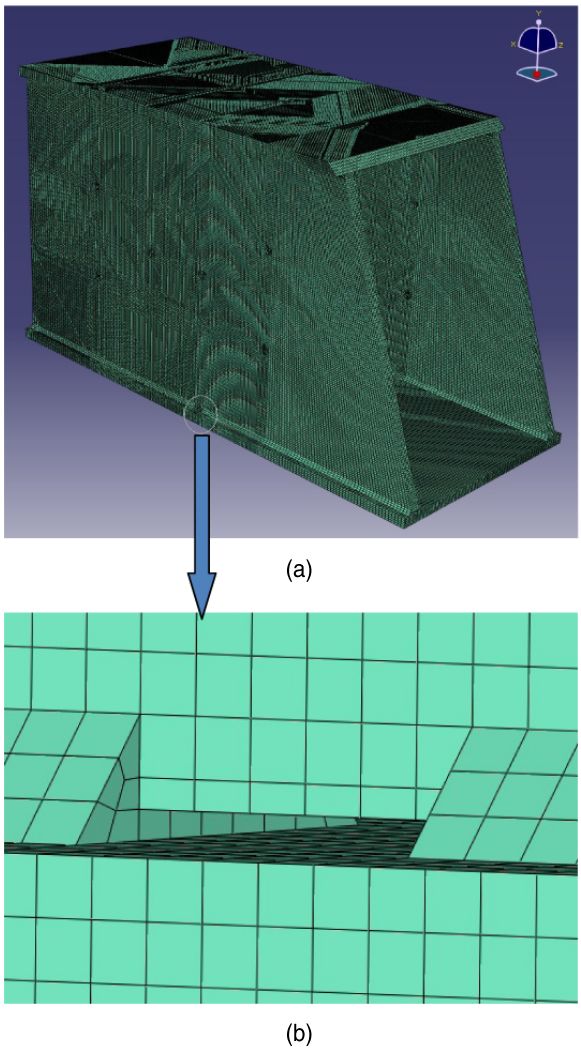

Figure 3. FEM model of the WTSS: (a) global view; and (b) zoomed-in part containing the simulated welding damage.

2.2. *FE simulation*

A three-dimensional FE model for the WTSS shown in figure 1(b) was developed using the commercial FE software ABAQUS®/CAE, in figure 3(a). The WTSS was modelled with three-dimensional eight-node solid brick elements (C3D8R in ABAQUS®). All the elements were set as 2 mm in three dimensions, guaranteeing that at least seven elements were allocated per wavelength of the transverse mode at any excitation frequency that would be used in this study. The welding damage was formed by removing associated FE elements from the meshed model (elements in the damage zone were resized to match the geometry of the damage) shown in figure 3(b).

The PZT wafer was simulated using a piezoelectric actuator/sensor model pre-developed by the authors elsewhere [29]. Uniform in-plane (x–y axis) displacement constraints, serving as excitation, were applied on FE nodes of the upper surfaces of the PZT actuator model, as shown in figure 4, in recognition of the mechanism of a PZT wafer. GW signals were activated using three-cycle *Hanning*-window-modulated sinusoid tonebursts at a central frequency of 150 kHz as incident wave signal, i.e., waveform of excitation. Dynamic simulation was carried out using commercial FE software ABAQUS®/EXPLICIT. The crack-reflected wave signals were captured by calculating the stress invariant at places where sensors were located. With the aim of ensuring calculation accuracy, the time interval of the calculation step was fixed at 4×10^{-8} s, which is much less than the time needed for GWs propagating across the minimum distance of any two adjacent nodes at the largest possible velocity.

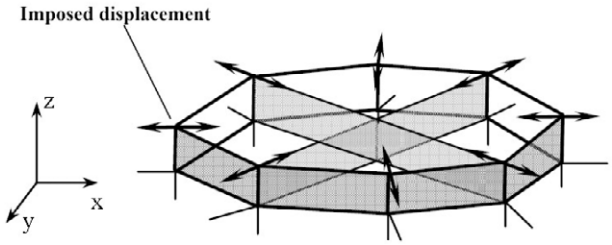

Figure 4. FEM model of the pre-developed GW actuator with uniform radial displacement constraints applied on circumferential FEM nodes.

2.3. *Propagation characteristics of GWs in WTSS*

As some typical results from simulation, snapshots for propagation of GWs generated by A_5 at several representative moments are exhibited in figure 5. From the simulation results, it can be concluded that GWs generated by a surface-bonded PZT actuator on any facet of the WTSS are confined within the same facet at first, as shown in figures 5(a) and (b); when incident GWs reach boundaries (welding zones and original edges of different facets of the WTSS), they are scattered (including wave reflection, transmission and diffraction) as seen obviously in figure 5(c); all the scattered wave components continue their propagation in adjacent facets. The simulation results have revealed that the propagation characteristics of GWs in a WTSS, though it is in the shape of tube, are similar to those propagating in a flat sheet (Lamb waves) in individual facets and different from those in a cylinder (cylindrical Lamb waves) [28] which are described by longitudinal, torsional and flexural modes.

Considering the above observation and location of the simulated welding damage, Facet C was deemed as the benchmark relative to Facet A, where a benchmark is referred to as the structure of the same dimension and properties but without any damage that is intentionally introduced. The introduced damage, deemed as extra boundary conditions of Facet A to GWs in comparison with the benchmark, modulates the propagation of GWs, leading to wave scattering. Comparing with baseline signals captured from the benchmark, pronounced changes in both waveform and amplitude can be observed, as shown in figure 6. For illustration, wave signals captured via two representative sensing paths, A_5A_2 and A_5A_6, and their corresponding benchmark counterpart, C_5C_2 and C_5C_6 (serving as baseline signals), are presented in figure 7. Although the amplitudes of signals from A_5A_2

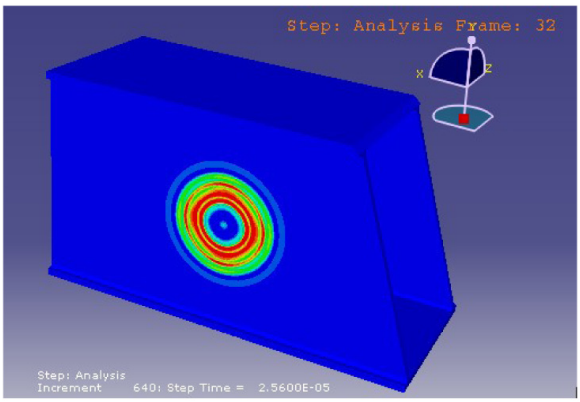

(a)

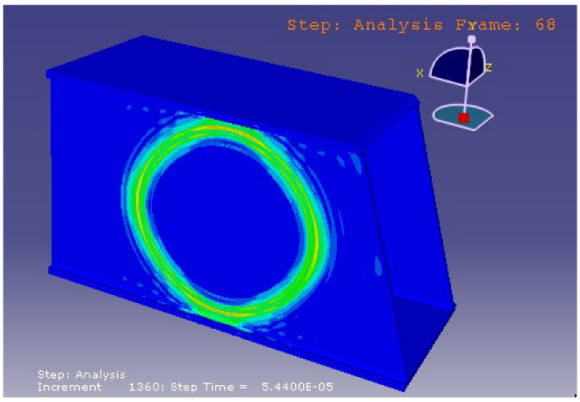

(b)

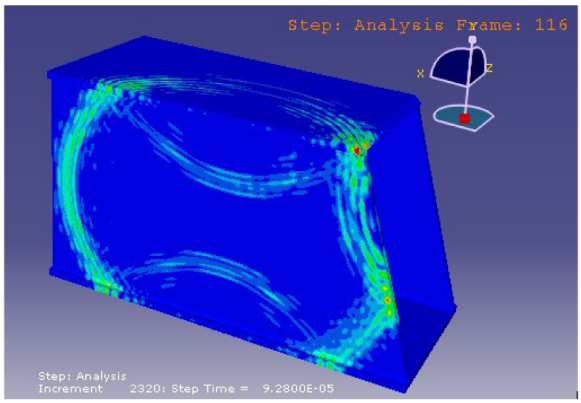

(c)

Figure 5. Snapshots for GW propagation in the WTSS at selected moments from FEM simulation: (a) 25.6 μs; (b) 54.4 μs; and (c) 92.8 μs.

and A_5A_6 changed in different ways in comparison with their baseline signals, becoming smaller in figure 7(a) and larger in figure 7(b), there is no doubt that the changes implied the occurrence of damage. Such changes, carrying damage information, were then used for evaluating the damage in the study. In addition, all the captured simulation signals will be processed before being employed for damage identification and the processing procedure will be stated in section 3.3.

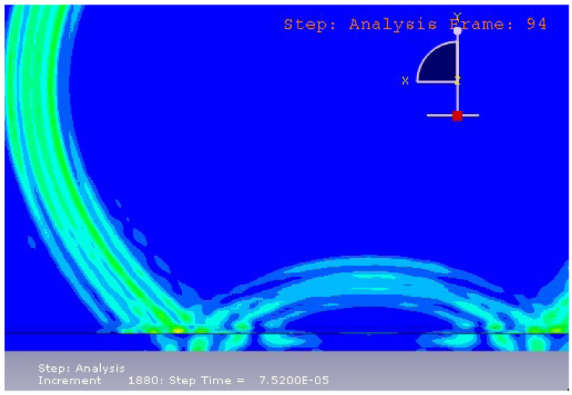

(a)

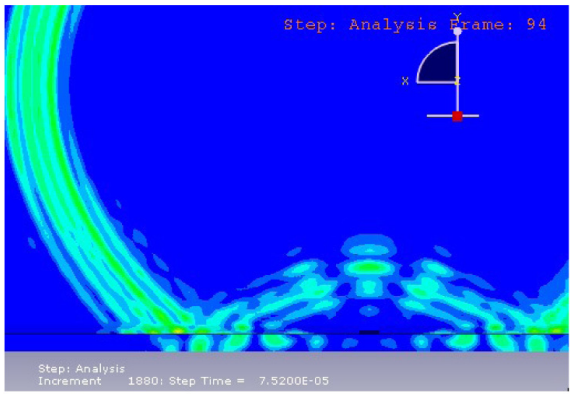

(b)

Figure 6. Wave scattering at the welding zone of the WTSS (a) without damage (benchmark), and (b) with the introduced slot-like damage.

3. Experiments

With the understanding of propagation characteristics of GWs in WTSSs with welding damage, an experiment was carried out with the purpose of identifying the welding damage.

3.1. Sample and equipment

Figure 8(a) shows a sample of the WTSS in figure 1(b). All the material properties and geometric dimensions, layout and nomenclature of PZT wafers in the active sensor network, as well as location and dimension of the welding damage remained unchanged from those in the above simulation. To simulate the damage, a welding defect, measuring about 12 mm (L) $\times$ 1 mm (W) $\times$ 10 mm (D), was introduced by keeping the corresponding location intact during the welding procedure, as shown in figure 8(b). Twelve PZT wafers, with their detailed properties listed in table 2, configured the active sensor network. The sample was supported along two free edges of Facet B on a TMC® testing table. Shielded wires and standard BNC connectors were used with the aim of reducing mutual interference. The excitation signals, three-cycle *Hanning*-window-modulated sinusoid tonebursts at selected central frequencies, were generated in MATLAB® and uploaded to an arbitrary waveform generator (HIOKI® 7075) in which D/A conversion was performed. Subsequently, the

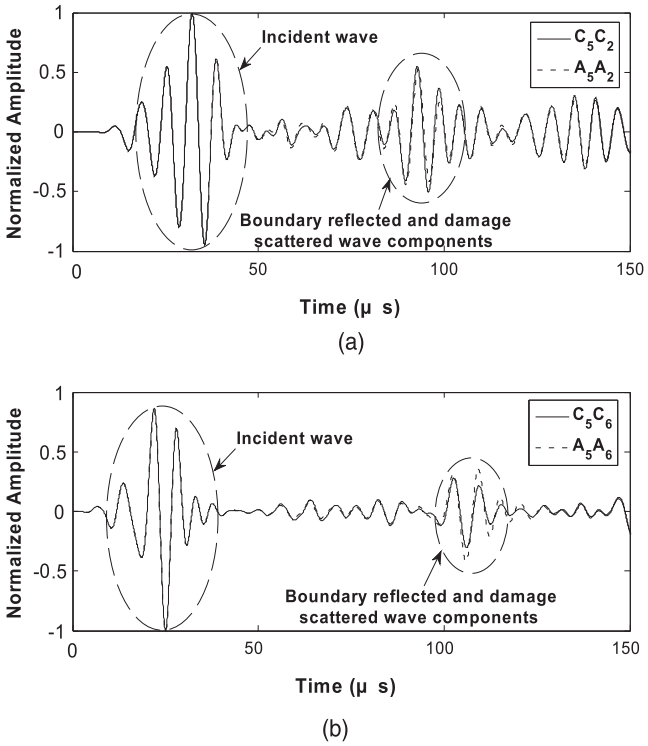

Figure 7. Comparison of raw signals captured in simulation captured via different sensing paths: (a) C_5C_2 (benchmark) and A_5A_2 (damaged); and (b) C_5C_6 (benchmark) and A_5A_6 (damaged).

Table 2. Mechanical and electrical properties of the PZT wafer used in the experiment.

Geometry	φ: 6.9 mm, thickness: 0.5 mm
Density	7.80 g cm^{-3}
Poisson's ratio	0.31
Charge constant, d_{31}	-170×10^{-12} m V^{-1}
Charge constant, d_{33}	450×10^{-12} m V^{-1}
Relative dielectric constant, K_3	1280
Dielectric permittivity, P_0	8.85×10^{-12} F m^{-1}
Elastic constant, E	72.5 GPa

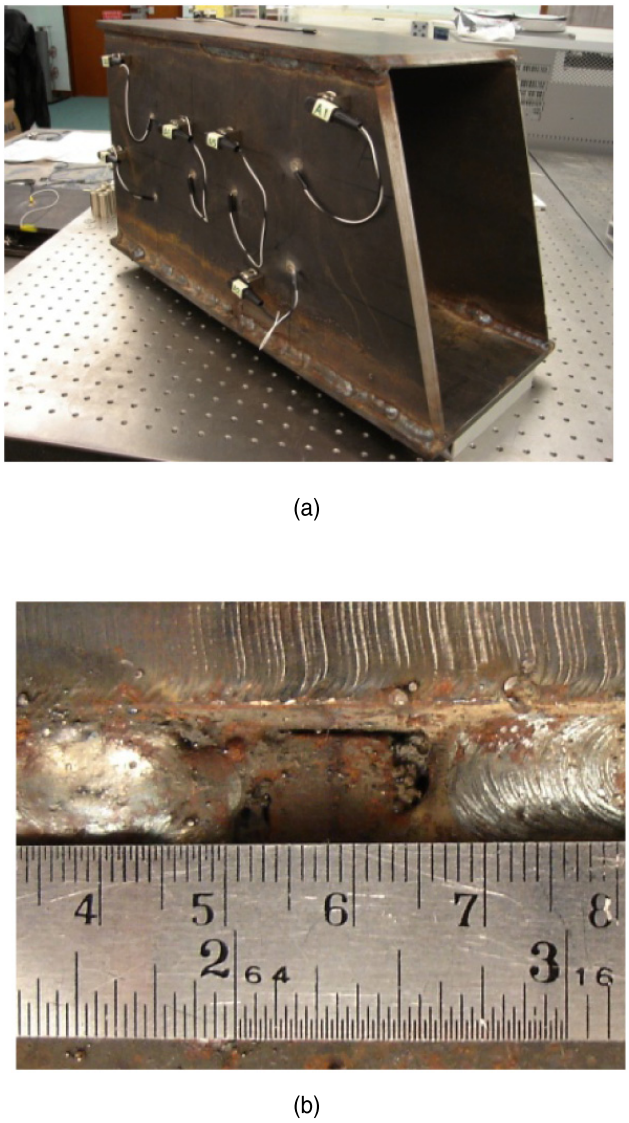

(a)

(b)

Figure 8. (a) Global view of the WTSS sample with emphasis on the active PZT sensor network on Facet A; and (b) zoomed-in part containing simulated welding damage.

analog signal was amplified by an amplifier (PiezoSys® EPA-104) to 80 V_{p-p} which was then applied on each PZT wafer in turn to activate GWs. When a PZT wafer was activated, the rest served as sensors to monitor the propagation of GWs in the WTSS using an oscilloscope (HP® Infinium 54810A) at a sampling rate of 10 MHz. In virtue of the high vertical sensitivity of this oscilloscope (1 mV/div.), relatively small difference in experimental signals can be distinguished since they are at least of several millivolts in the current study.

3.2. Excitation frequency and wave velocity

In terms of the dispersive properties of GWs in steel [28], the excitation frequency of GW must be small enough in order to avoid emergence of higher-order GW modes which complicate the signal appearance and make it hard to extract signal features. In contrast, excitation of excessively low frequencies causes a very large wavelength and accordingly low time resolution of the signal, and as a result the sensitivity of the wave to damage is reduced. Moreover, different wave modes in a wave signal at different frequencies may have different shares of the overall signal energy. To address these concerns, a sweep frequency test was conducted to investigate the performance of excitations at a frequency range from 80 to 250 kHz with a step of 5 kHz. It was found that the amplitude of the wave signals was too small to be distinguished from background noise when the excitation frequencies were in the range of 80–120 kHz, but the amplitude became recognizable when the excitation frequency was over 120 kHz, and in particular strong at 150, 175 and 200 kHz, facilitating enhancement of the signal-to-noise ratio. Balancing the observability and handleability of the collected signals, three-cycle *Hanning*-window-modulated sinusoid tonebursts at 150, 175 and 200 kHz were utilized as excitations in both experiments and simulations.

In a preparatory test the wave components scattered by damage were often observed to overlap those reflected from

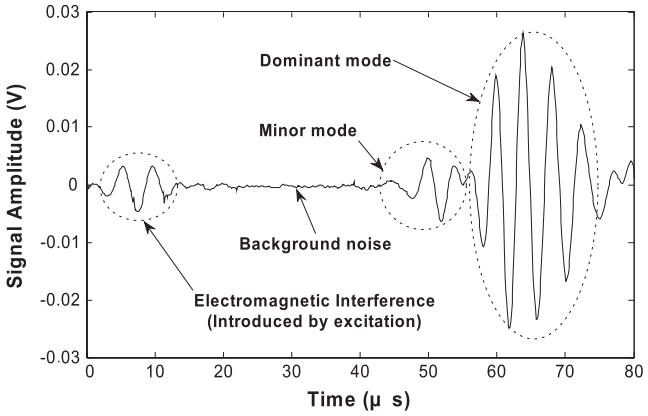

Figure 9. A typical raw signal from sensing path C_4C_5 in the preparatory test.

boundaries of the WTSS, because the damage is located near physical edges of the WTSS. At the same time, different wave modes existed in all captured signals. Though stimulated using excitations at carefully selected frequencies of 150, 175 and 200 kHz so as to avoid interference from multiple modes in a GW signal, interaction of multiple wave modes was unavoidable. Therefore, it is difficult to clearly distinguish different wave components in captured GW signals. Thanks to the relatively large magnitude, the dominant modes, the above-mentioned transverse modes, in signals could be isolated from other signal components, like one example shown in figure 9. The two modes in this figure are wave components that travelled directly from actuator to sensor and the minor one can be recognized as a longitudinal mode that propagated faster. Through the preparatory test, the velocity of the dominant GW mode in the sample, V_d, was also calculated by dividing the distance between actuator and sensor by the difference between the arrival times of the excitation and dominant mode in the corresponding sensing path, e.g. 276.6 mm and 90.5 μs for A_1A_3, and was determined as about 2950 m s^{-1} after averaging results from multiple paths.

3.3. Experiment and signal processing

Experiments were conducted according to the configuration introduced above. The same procedure was repeated with excitations of different central frequencies. As observed in both FE simulation (section 2.3) and experiment (section 3.2), captured GW signals in WTSSs are often complex in appearance, posing difficulty in damage identification. A series of signal processing was applied, including signal pre-processing (averaging), CWT and HT (please refer to [30] for detailed algorithms and expressions), with the aim of de-noising and feature highlighting. For brief illustration, only raw and processed signals will be shown hereafter with derivations omitted. Furthermore, in order to avoid the extra influence of opposite-boundary reflections and circumferential transmission on signal interpretation, only the first few components of each GW signal were taken into account. Such truncation was applied to each collected signal, ensuring the absence of those unwanted wave components.

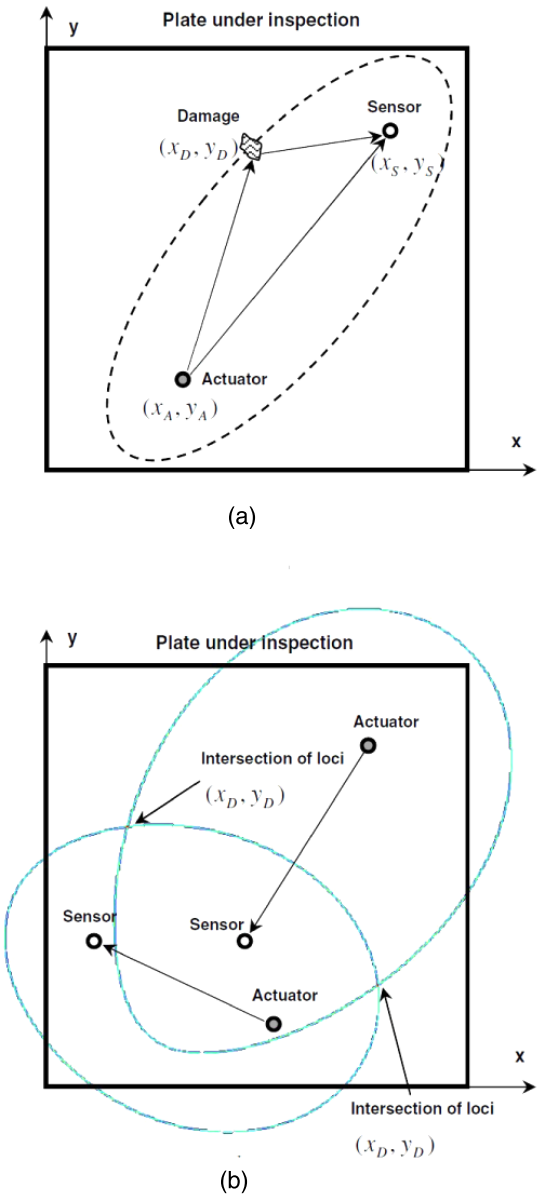

(a)

(b)

Figure 10. ToF-based triangulation of damage in a two-dimensional plate with two sensing paths: (a) locus established by one sensing path; and (b) two loci established by two paths.

4. Identification of welding damage in a WTSS

4.1. Traditional ToF-based methods

Damage-scattered GW components carry damage information, which, upon a series of signal processing, can be used for identifying damage. In many studies [9, 12, 31], a signal feature, time-of-flight (ToF), is often used to triangulate damage. The difference in ToFs, defined as the time lag between the incident wave that the sensor first captures and the wave scattered by damage that the same sensor subsequently captures, substantially suggests the relative positions among the actuator, sensor and damage. From such difference in the ToFs extracted from a certain number of signals, damage can accordingly be triangulated. To briefly give the principle, consider a two-dimensional plate with a sensing path, as shown in figure 10(a). One can obtain the following equation:

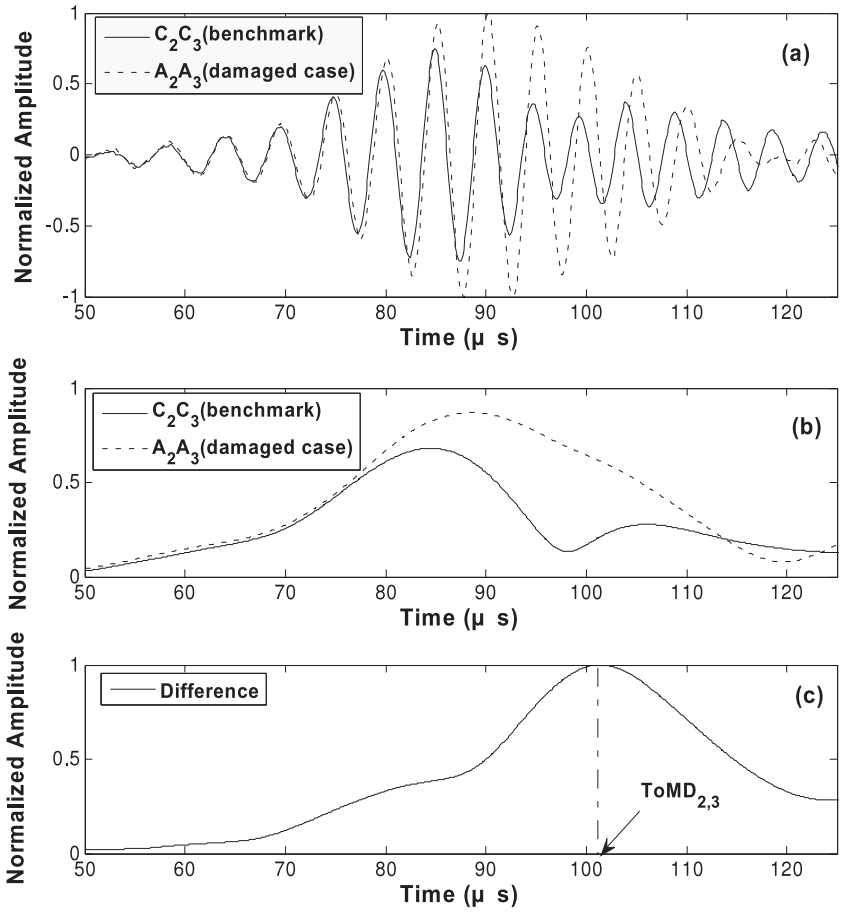

Figure 11. Normalized signals for sensing path pair $P_{2,3}$ under excitation at 150 kHz: (a) raw signals; (b) envelope of corresponding CWT coefficients; and (c) envelope of the difference signal.

$$\Delta t = t_{\mathrm{A-D-S}} - t_{\mathrm{A-S}} = \left(\frac{D_{\mathrm{A-D}} + D_{\mathrm{D-S}}}{V}\right) - \frac{D_{\mathrm{A-S}}}{V}, \quad (1)$$

where

$$D_{\mathrm{A-D}} = \sqrt{(x_{\mathrm{D}} - x_{\mathrm{A}})^2 + (y_{\mathrm{D}} - y_{\mathrm{A}})^2},$$

$$D_{\mathrm{D-S}} = \sqrt{(x_{\mathrm{S}} - x_{\mathrm{D}})^2 + (y_{\mathrm{S}} - y_{\mathrm{D}})^2},$$

$$D_{\mathrm{A-S}} = \sqrt{(x_{\mathrm{S}} - x_{\mathrm{A}})^2 + (y_{\mathrm{S}} - y_{\mathrm{A}})^2}.$$

In the above equation, $t_{\mathrm{A-D-S}}$ is the ToF of the incident wave propagating from the actuator to the damage and then to the sensor, and $t_{\mathrm{A-S}}$ is the ToF of the incident wave propagating directly from the actuator to the sensor. Δt is the difference between the above two ToFs, which can be extracted from the captured GW signal. $D_{\mathrm{A-D}}$ is the distance between the actuator located at $(x_{\mathrm{A}}, y_{\mathrm{A}})$, and the damage centre, presumed at $(x_{\mathrm{D}}, y_{\mathrm{D}})$ and to be determined; $D_{\mathrm{D-S}}$ is the distance between the damage centre and the sensor located at $(x_{\mathrm{S}}, y_{\mathrm{S}})$; $D_{\mathrm{A-S}}$ is the distance between the actuator and sensor. V is the group velocity of the incident GW activated by the actuator and the GW scattered by the damage. Theoretically, the solutions to equation (1) configure a locus, a dotted line in figure 10(a), indicating possible locations of the centre of the damage. With ToF extracted from another sensing path, an equation similar to equation (1) can be obtained, and a nonlinear equation group, containing two equations contributed by two sensing paths and involving the position of the damage centre $(x_{\mathrm{D}}, y_{\mathrm{D}})$ (two unknown variables), is available. Two loci established by the two equations lead to intersection(s), i.e., the solution(s) to the equation group, sketched in figure 10(b), which is (are) the location(s) of the damage centre $(x_{\mathrm{D}}, y_{\mathrm{D}})$.

However it is envisaged that, because of the complex superposition of various wave components in the WTSS mentioned above and allowing for measurement noise/uncertainties under demanding operational conditions, it is highly impossible to exactly locate damage based on the above-addressed procedure.

4.2. ToMD and DPP-based damage imaging

In recognition of the fact that Facets A and C of the sample are entirely symmetrical regarding the symmetry plane as shown in figure 1(b) not only in geometry but also in active sensor network configuration, differences, if any, between captured GW signals from corresponding sensing paths of two facets can be fully attributed to the damage. For convenience of discussion, $P_{m,n}$ $(m, n = 1, 2, \ldots, 6, m \neq n)$ hereafter stands for the arbitrary sensing path pair consisting of the sensing path A_mA_n and its corresponding benchmark counterpart C_mC_n.

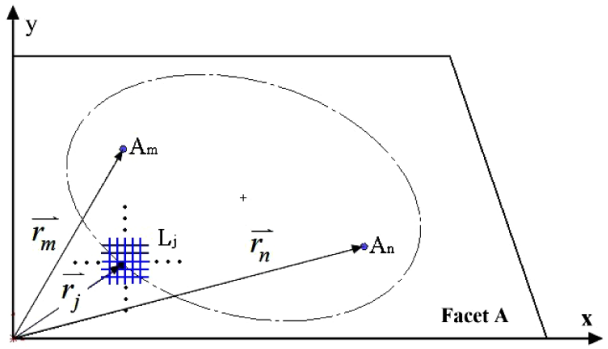

Figure 12. ToMD-based determination of DPP on Facet A of the WTSS.

For a given $P_{m,n}$, two raw GW signals were captured (one via C_mC_n and the other via A_mA_n). After applying averaging and CWT to raw signals, as described in section 3.3, HT was subsequently employed to obtain the envelope of the difference signal to highlight features of the signal in the time domain, i.e., amplitude peaks and their corresponding arrival times. In the envelope of the difference signal, the arrival time of local amplitude maximum was termed *time of maximal difference* (ToMD) in regard to $P_{m,n}$, denoted by $\text{ToMD}_{m,n}$ in what follows. Representatively, $\text{ToMD}_{m,n}$ extracted from raw signals experimentally captured via $P_{2,3}$ (i.e., $\text{ToMD}_{2,3}$) is shown in figure 11.

Instead of exactly locating the damage, this study focused on determining *damage presence probabilities* (termed DPPs) at all locations on the WTSS. The following imaging algorithm was developed to calculate DPP value(s) for arbitrary location(s) of the WTSS and firstly applied to Facet A. Without loss of generality, supposing that Facet A was meshed virtually using K grids (e.g., 1×1 mm^2 each in the following), the distance from a certain grid L_j $(j = 1, 2, \ldots, K)$ to PZT wafer A_m can be expressed as $D_{m,j} = |\vec{r_m} - \vec{r_j}|$ where $\vec{r_m}$ and $\vec{r_j}$ are location vectors of A_m and L_j in the global coordinate system, as shown in figure 12. The time needed for GWs to travel along the route $A_m \rightarrow L_j \rightarrow A_n$ can then be defined as $T_{m,j,n} = (D_{m,j} + D_{n,j})/V_d$. Similar to equation (1) in the above section, for the equation

$$\text{ToMD}_{m,n} - T_{m,j,n} = 0, \tag{2}$$

the coordinates of the damage centre are two unknown variables. The solution of equation (2) presented an ellipse locus with the two PZT wafers being two foci, as portrayed with a dash-dotted line in figure 12. In principle, the grids that correctly locate on this locus, i.e., their coordinates can satisfy equation (2), have the highest probability of bearing damage from the prospect of the sensing path pair $P_{m,n}$ that produces such a locus. Therefore, the DPP values of these grids were determined as 100%.

For grids at other locations, their coordinates can never satisfy equation (2). The further these grids are away from the ellipse locus, the less the probability that they bear damage. In this sense, to quantify the DPP values at such grids in relation to their locations L_j $(j = 1, 2, \ldots, K)$ and sensing path pair $P_{m,n}$ $(m, n = 1, 2, \ldots 6, m \neq n)$, a *cumulative distribution function* (CDF) [32] defined as

$$F_{m,n}(t) = \int_{-\infty}^{t} f(T'_{m,j,n})\, \mathrm{d}T'_{m,j,n} \tag{3}$$

was then introduced where $f(T'_{m,j,n}) = \frac{1}{\sigma_{m,n}\sqrt{2\pi}} \exp[-\frac{(T'_{m,j,n})^2}{2\sigma^2_{m,n}}]$ is the *Gaussian distribution function*, representing the density function of the DPP. In the above equation, $T'_{m,j,n} = |\text{ToMD}_{m,n} - T_{m,j,n}|$ is a function of L_j when $\text{ToMD}_{m,n}$ is given, denoting the 'distance' between grid L_j and the ellipse locus in time domain. $\sigma_{m,n}$ is the standard variance and the integral upper limit t is the value of $T'_{m,j,n}$ when m, j, n are specified. Given a $T'_{m,j,n}$, the DPP value of grid L_j regarding $P_{m,n}$ becomes

$$\text{DPP}(L_j, P_{m,n}) = 1 - |F_{m,n}(T'_{m,j,n}) - F_{m,n}(-T'_{m,j,n})| \tag{4}$$

as exhibited in figure 13.

Applying the above algorithm to all grids on Facet A, an image for the estimated values of $P_{m,n}$ involved DPP can be obtained. After extending such a process to all other facets of the WTSS, a three-dimensional DPP image was constructed where damage was intuitionally visualized. As a

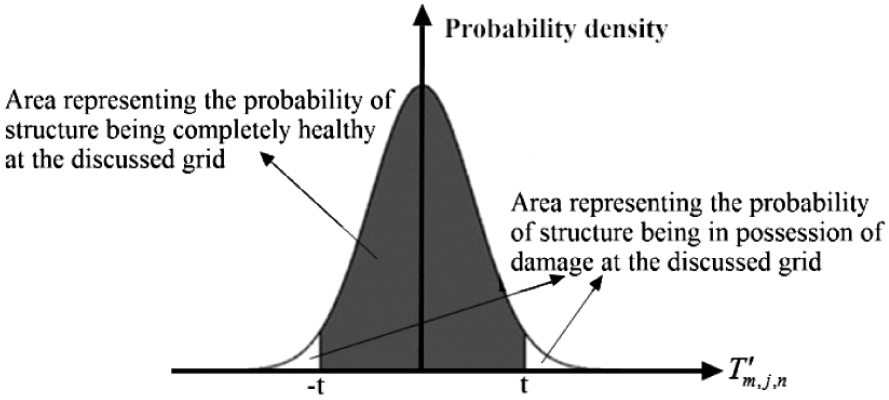

Figure 13. Gaussian distribution of the probability density in regard to the occurrence of damage at a specific grid of the WTSS.

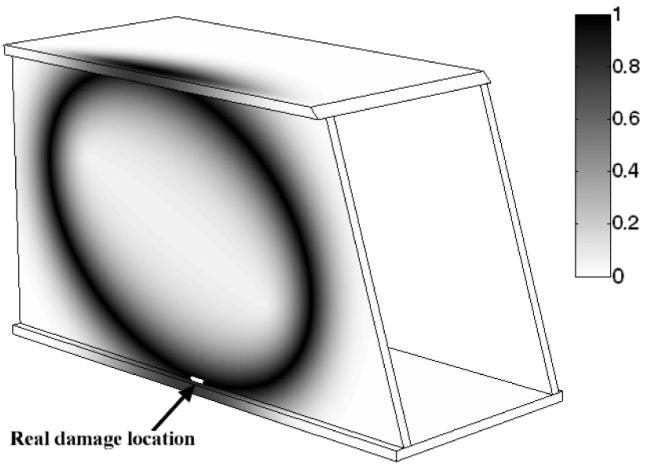

Figure 14. DPP image contributed by $P_{2,4}$ (from experiment).

typical experimental result, the DPP image contributed by $P_{2,4}$ is illustrated in figure 14. In this image, DPP values vary within the range of [0, 1] (indicated by grey-scale colours shown in the colour bar) with the two extremes standing for the lowest and highest DPP, i.e., 0% and 100%, respectively. Similar to some other recently developed imaging techniques for describing a damage event in engineered structures [23, 33–36], the darker the grey-scaled image appears, the greater the DPP of this grid is. Figure 14 suggested that the possible form of the damage is a large elliptical ring because all grids on the central line of the darkest region are of the same DPP value. In fact, damage cannot shape such a profile in real applications. The unrealistic estimation result indicated the insufficiency of determining the damage location by information from a single sensing path pair. Therefore, images contributed by all the available $P_{m,n}$ in the active sensor network were fused to configure out the common estimate of the damage location.

4.3. Two-level hybrid image fusion scheme

To strengthen the damage-associated information in the final estimation result, a two-level hybrid image fusion scheme was proposed based on conjunctive and compromised image fusion techniques. For simplicity, DPP images established by all the available $P_{m,n}$ were sorted according to the wave excitation frequency (150, 175 and 200 kHz), denoted by Set-150k, Set-175k and Set-200k, respectively. Image fusion procedures within each image set and across sets, namely, the first and second level image fusions, were taken successively.

4.3.1. First level fusion. Taking Set-150k as an example, algebraic operations were applied to DPP values of all images in Set-150k using conjunctive and compromised fusion techniques which are respectively defined as

$$Conj\_DPP\_150k(L_j, P) = \sqrt[N_P]{\prod_{m,n\in\{1,2,\ldots,6\}}^{m\neq n} DPP(L_j, P_{m,n})}, \quad j = 1, 2, \ldots, K \tag{5a}$$

Table 3. Set P: sensing path pairs involved in the first level image fusion.

(A_1A_2, C_1C_2)	(A_3A_1, C_3C_1)	(A_5A_1, C_5C_1)
(A_1A_3, C_1C_3)	(A_3A_2, C_3C_2)	(A_5A_2, C_5C_2)
(A_1A_4, C_1C_4)	(A_3A_4, C_3C_4)	(A_5A_3, C_5C_3)
(A_1A_5, C_1C_5)	(A_3A_5, C_3C_5)	(A_5A_4, C_5C_4)
(A_1A_6, C_1C_6)	(A_3A_6, C_3C_6)	(A_5A_6, C_5C_6)
(A_2A_1, C_2C_1)	(A_4A_1, C_4C_1)	(A_6A_1, C_6C_1)
(A_2A_3, C_2C_3)	(A_4A_2, C_4C_2)	(A_6A_2, C_6C_2)
(A_2A_4, C_2C_4)	(A_4A_3, C_4C_3)	(A_6A_3, C_6C_3)
(A_2A_5, C_2C_5)	(A_4A_5, C_4C_5)	(A_6A_4, C_6C_4)
(A_2A_6, C_2C_6)	(A_4A_6, C_4C_6)	(A_6A_5, C_6C_5)

$$Comp\_DPP\_150k(L_j, P) = \frac{1}{N_P}\sum_{m,n\in\{1,2,\ldots,6\}}^{m\neq n} DPP(L_j, P_{m,n}), \quad j = 1, 2, \ldots, K \tag{5b}$$

where P is the set of all involved sensing path pairs, as listed in table 3; N_P is the number of elements in set P and is equal to 30 in this study. '*Conj_DPP_150k*' and '*Comp_DPP_150k*' are so-called first level fusion results for Set-150k. Similarly, the same operation was applied to Set-175k and Set-200k. Figures 15 and 16 show the first level image fusion results from simulation and experiment data, respectively. DPP values in these fused images, as well as in the following ones, were normalized in regard to the maximal DPP value of the current image, ensuring that the DPP values are always in the range [0, 1].

In these two figures, dark areas representing estimated welding damage at the welding zone between Facets A and B are clearly observed. From all the subfigures we can see that, referring to the real damage which is shown in contrast colour, the estimated damage (the darkest area) in each image can more or less cover the real damage spot, indicating the effectiveness of the recommended approach. Also, comparing figure 15 with figure 16, an obvious similarity can be found, hinting that the predicted results from simulations and experiments can match well. Moreover, although different columns (representing different fusion techniques) in the same figure offer predicted results in different views, the darkest areas maintain a relative constant location. As for the precision of different fusion techniques and different excitation frequencies, table 4 gives us a clear view and more details will be addressed later in section 4.3.3.

4.3.2. Second level fusion. In order to enhance the accuracy of the estimate result by properly employing as much useful information as possible, the second level image fusion, i.e., fusion across DPP image sets for different excitations, was undertaken. Both conjunctive and compromised schemes were utilized again to combine the first level image fusion results. By applying different strategies, four joint schemes were established and are expressed below:

$$Comb\_DPP\_S1 = \sqrt[3]{\prod_{Freq\in\{150k,175k,200k\}} Conj\_DPP\_Freq} \tag{6a}$$

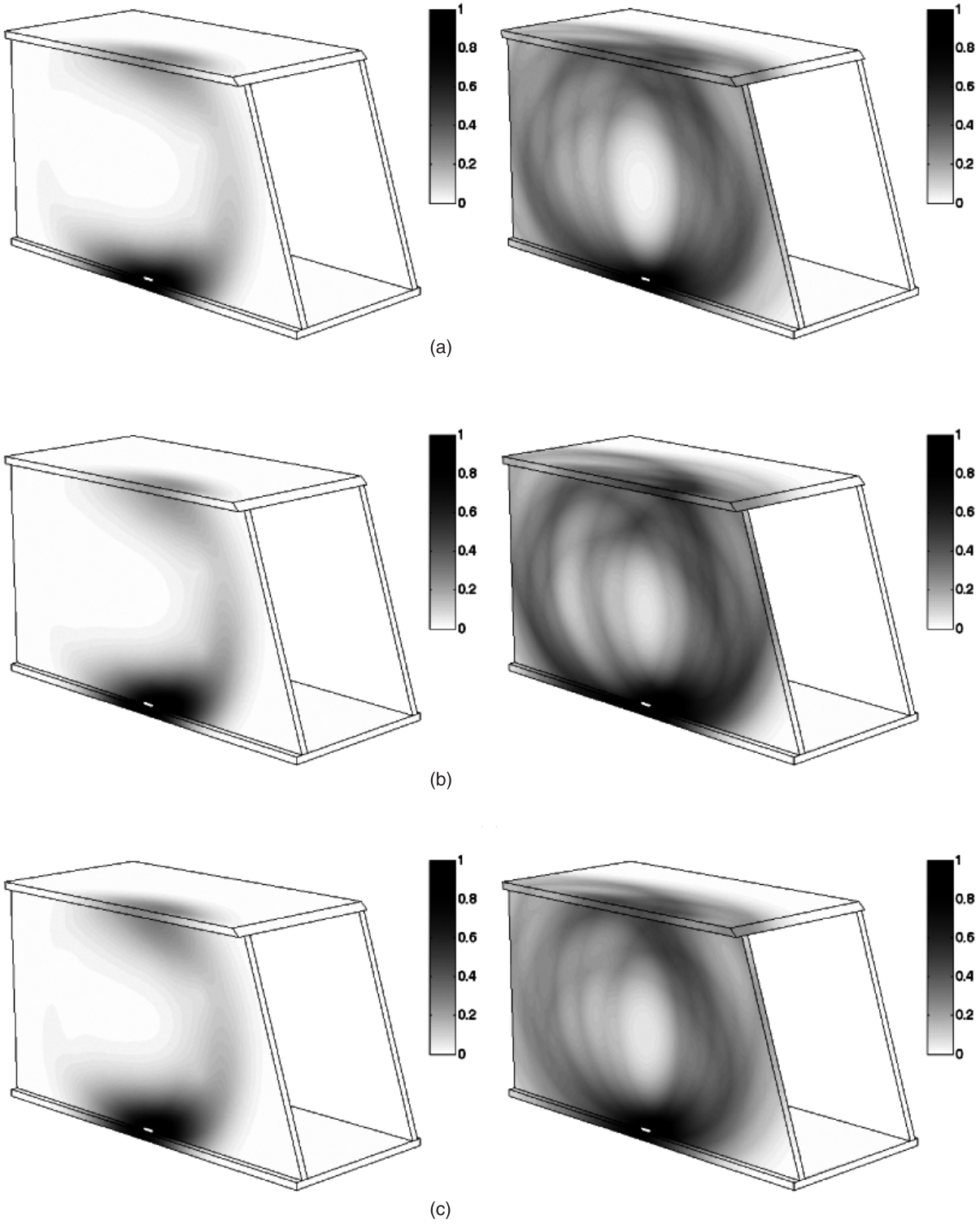

Figure 15. Fused DPP images based on the first level image fusion (from simulation) for (a) Set-150k; (b) Set-175k; and (c) Set-200k using conjunctive (left) and compromised (right) schemes.

$$Comb\_DPP\_S2 = \frac{1}{3} \sum_{\text{Freq}\in\{150k,175k,200k\}} Conj\_DPP\_Freq \quad (6b)$$

$$Comb\_DPP\_S3 = \sqrt[3]{\prod_{\text{Freq}\in\{150k,175k,200k\}} Comp\_DPP\_Freq} \quad (6c)$$

$$Comb\_DPP\_S4 = \frac{1}{3} \sum_{\text{Freq}\in\{150k,175k,200k\}} Comp\_DPP\_Freq \quad (6d)$$

where S1–S4 on the LHS stand for purely conjunctive, conjunctive–compromised, compromised–conjunctive, and purely compromised schemes in turn. Figures 17 and 18 show the results of the second level image fusion from simulation

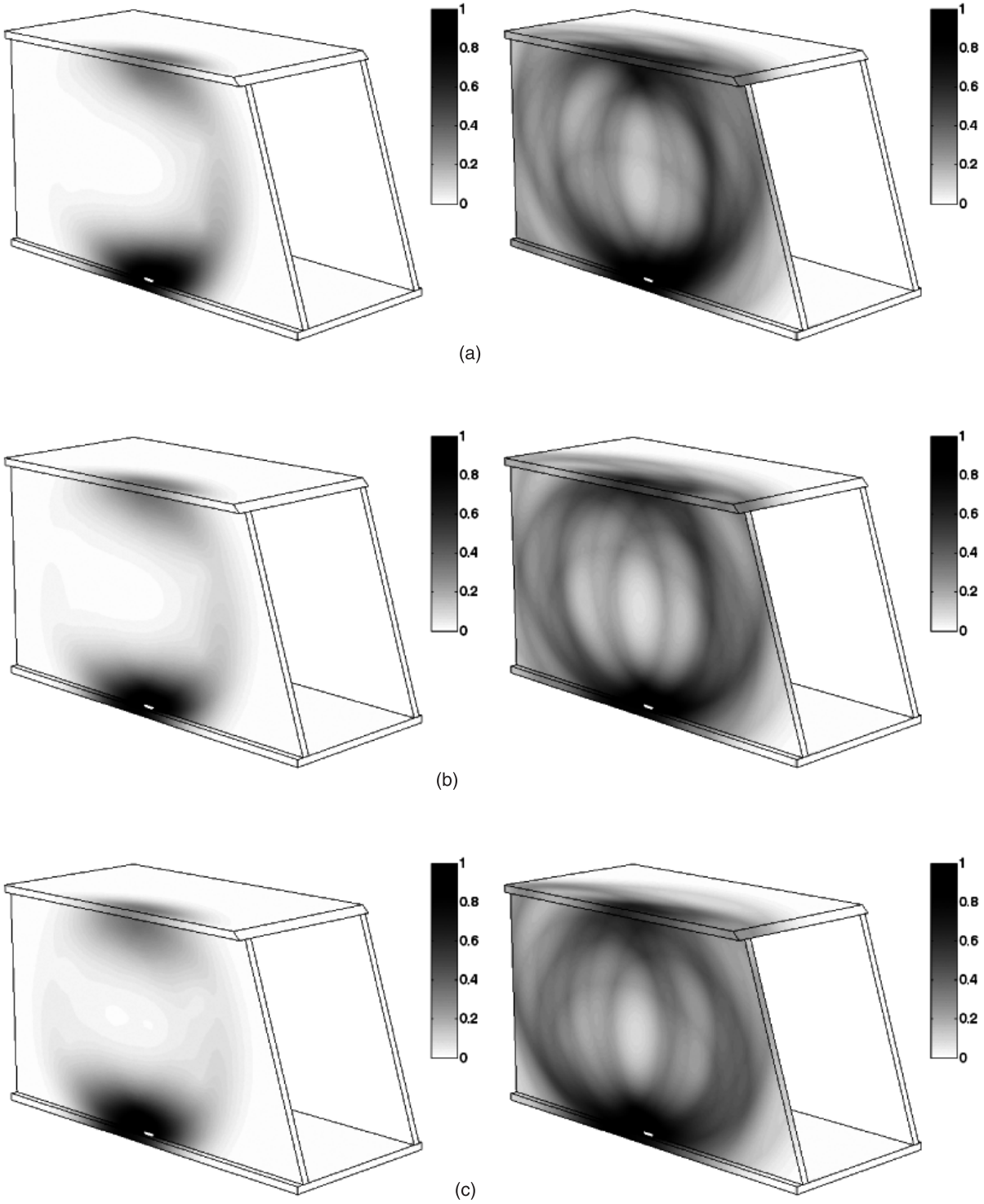

Figure 16. Fused DPP images based on the first level image fusion (from experiment) for (a) Set-150k; (b) Set-175k; and (c) Set-200k using conjunctive (left) and compromised (right) schemes.

and experiment data, respectively. In the images, in spite of the characteristics similar to those in figures 15 and 16, approach of the estimated damage location to the real one, though not very obvious due to the large dimensions of the WTSS, can be found, as detailed in section 4.3.3. Meanwhile, DPP images for '*Comb_DPP_S1*' and '*Comb_DPP_S3*', as well as those for '*Comb_DPP_S2*' and '*Comb_DPP_S4*', can be found to be highly accordant, implying the robustness of the second level fusion.

4.3.3. Analysis of fusion results. Locations with the highest probability of damage occurrence in figures 15–18 were picked out and detailed in table 4. The coordinate system is the same as that indicated in figure 1(b). The distances between

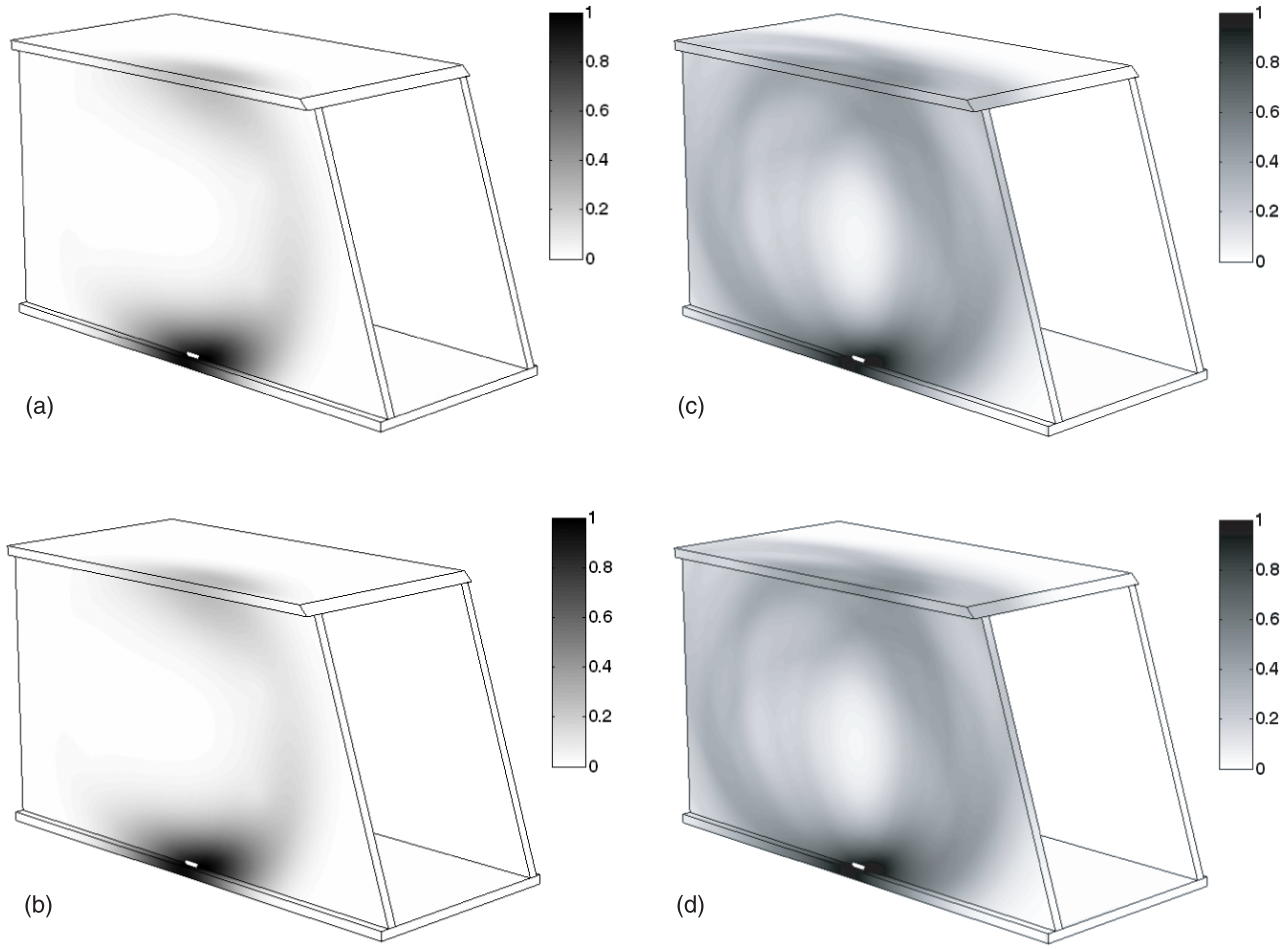

Figure 17. Fused DPP images based on the second level image fusion (from simulation) using (a) purely conjunctive; (b) conjunctive–compromised; (c) compromised–conjunctive and (d) purely compromised schemes.

Table 4. Estimated damage locations from the two-level fusion procedure.

		Estimated results from simulation			Estimated results from experiment		
	Case	Coordinates (mm)	Distance to real location (mm)	Relative error (%)	Coordinates (mm)	Distance to real location (mm)	Relative error (%)
	Real damage location	(275, 0, 0)	—	—	(275, 0, 0)	—	—
First level fusion	*Conj_DPP_150k*	(276, 0, −8)	8.1	2.95	(282, 8, 0)	10.6	3.85
	Conj_DPP_175k	(291, 0, −1)	16.0	5.82	(270, 6, 0)	7.8	2.84
	Conj_DPP_200k	(281, 4, 0)	7.2	2.62	(253, 10, 0)	24.2	8.80
	Comp_DPP_150k	(275, 0, −7)	7.0	2.55	(282, 8, 0)	10.6	3.85
	Comp_DPP_175k	(291, 0, −1)	16.0	5.82	(281, 8, 0)	10.0	3.64
	Comp_DPP_200k	(281, 4, 0)	7.2	2.62	(260, 14, 0)	20.5	7.45
Second level fusion	*Comb_DPP_S1*	(280, 0, −2)	5.4	1.96	(269, 6, 0)	8.5	3.09
	Comb_DPP_S2	(280, 0, −2)	5.4	1.96	(269, 6, 0)	8.5	3.09
	Comb_DPP_S3	(278, 0, −3)	4.2	1.53	(276, 7, 0)	7.1	2.58
	Comb_DPP_S4	(278, 0, −3)	4.2	1.53	(276, 7, 0)	7.1	2.58

estimated locations and the real damage position, as well as relative errors which are ratios of these distances to that between the real damage location and the origin, are also included in this table. It is found that: (1) comparing with the sample dimensions, the distances between estimated locations and the real one are relatively small, implying the acceptability of the proposed approach; (2) whichever fusion schemes were adopted in the two-level fusion procedure, obvious improvement in identification accuracy can be observed when the second level fusion is applied, validating its necessity; and (3) although not every result of the second level fusion is more accurate than those based on solely first level fusion, a more convincing decision can be drawn from the two-level data fusion procedure.

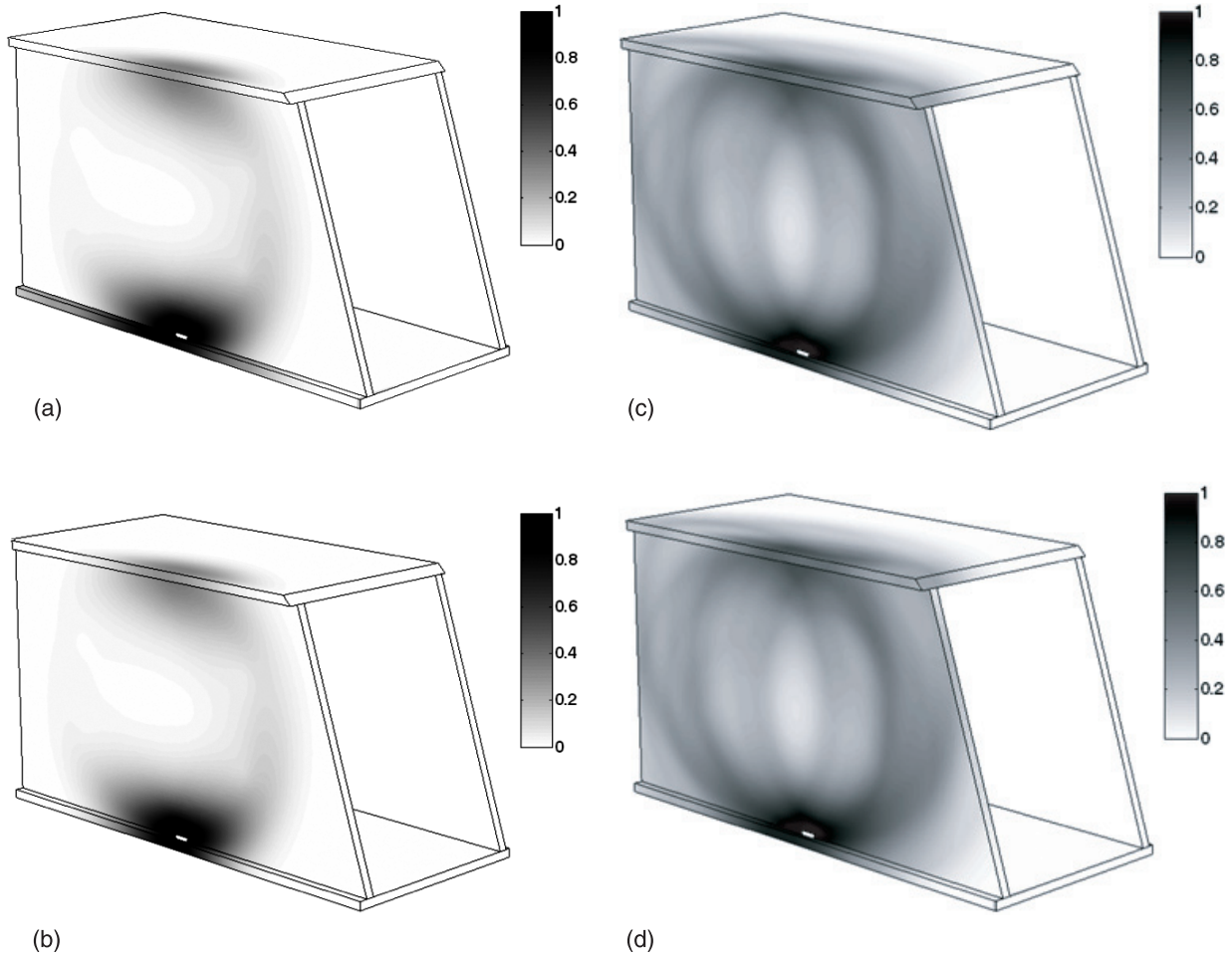

Figure 18. Fused DPP images based on the second level image fusion (from experiment) using (a) purely conjunctive; (b) conjunctive–compromised; (c) compromised–conjunctive and (d) purely compromised schemes.

4.4. Analysis of error

The arithmetic of DPP stated in section 4.2 is sensitive to ToMD. Any factor that can affect the ToMD value may lead to error in the DPP image derived from the single sensing path pair. Such error could be amplified during the subsequent data fusion procedure, especially under schemes containing conjunctive operation(s) [37]. In this study, many factors would affect the final fusion results of the experiments. Firstly, uncertainties, such as the disparity in geometry between Facets A and C (despite the introduced damage), variation of welding quality, etc, are almost unavoidable. Secondly, weld ends, besides the induced damage, enlarge the expected damage zone so that the consequent fusion results would be affected. Thirdly, the time duration of the wave component of interest in the received signal is always longer than its original form due to the intrinsic dispersion characteristic of the GWs utilized. However, in virtue of the advantages of two-level data fusion, the errors from the different first level fusion results are somewhat diminished. Taking all these matters into consideration, the fused results for damage location, as well as their relative errors listed in table 4, are acceptable.

5. Conclusion

Propagation behaviour of GWs in a WTSS, a true-scale model of a train bogie frame segment containing slot-like welding damage, was investigated in this study under the hypothesis that the WTSS is homogeneous. The damage-scattered wave components carrying damage information were mainly considered. An active sensor network consisting of twelve PZT wafers was established to activate or collect GWs in the WTSS. Excitations at different frequencies were used to obtain rich signals for investigation. An imaging approach based on GW propagation and concepts, ToMD and DPP, was developed for estimation of damage presence and location. A two-level image fusion scheme was further proposed with the aim of enhancing the robustness of the approach to measurement noise and uncertainties. From the results for estimation of damage location, it can be concluded that, although the damage was located within the welding zone and near the original edges of the WTSS, making damage evaluation much more difficult, acceptable estimation results of damage location can still be gained by applying the proposed imaging approach and the first level image fusion. Additional improvements in consistency and accuracy of the damage evaluation results were achieved when the second level fusion

was performed. In brief, acceptable visualized evaluation of slot-like damage in the welding zone of a WTSS was accomplished using an approach combining GW propagation based imaging and a two-level image fusion procedure, indicating the effectiveness of the recommended approach in evaluating presence and location of such welding damage in WTSSs and its large potential for real-time SHM of WTSSs. In addition, consideration of nonhomogeneity of the material properties and its potential impact on the characteristics of waves propagating in WTSSs will be addressed in future work.

Acknowledgments

The authors are grateful for the support received from the Research Grant Council of the Hong Kong Special Administration Region (grant: PolyU5333/07E) and the Hong Kong Polytechnic University (grants: G-U204, 1-BBZN and A-PE1F).

References

[1] National Aeronautics and Space Administration (NASA) 2007 Derailed *Syst. Failure Case Stud.* **1** 1–4
[2] MTR Co. Ltd 2007 *Circular for Rail Merger* available from: http://www.mtr.com.hk/eng/investrelation/circulars2007/ew%200066cir%2020070903.pdf
[3] Achenbach J D 2000 Quantitative nondestructive evaluation *Int. J. Solids Struct.* **37** 13–27
[4] Gray J and Tillack G-R 2001 X-ray imaging methods over the last 25 years—new advances and capabilities *Review of Progress in Quantitative Nondestructive Evaluation* vol 557A ed D O Thompson and D E Chimenti (New York: American Institute of Physics) pp 16–32
[5] Balageas D L 2002 Structural health monitoring R&D at the 'European Research Establishments in Aeronautics' (EREA) *Aerospace Sci. Technol.* **6** 159–70
[6] Sohn H, Farrar C R, Hemez F M, Shunk D D, Stinemates D W and Nadler B R 2003 Review of structural health monitoring literature: 1996–2001 *Los Alamos National Laboratory Report* LA-13976-MS
[7] Boller C 2001 Ways and options for aircraft structural health management *Smart Mater. Struct.* **10** 432–40
[8] Alleyne D N and Cawley P 1992 The interaction of Lamb waves with defects *IEEE Trans. Ultrason. Ferroelectr. Freq. Control* **39** 381–97
[9] Kessler S S, Spearing S M and Soutis C 2002 Damage detection in composite materials using Lamb wave methods *Smart Mater. Struct.* **11** 269–78
[10] Staszewski W J, Boller C and Tomlinson G R 2004 *Health Monitoring of Aerospace Structures: Smart Sensor Technologies and Signal Processing* (New York: Wiley)
[11] Raghavan A and Cesnik C E S 2007 Review of guided-wave structural health monitoring *Shock Vib. Dig.* **39** 91–114
[12] Giurgiutiu V and Bao J 2004 Embedded-ultrasonics structural radar for *in situ* structural health monitoring of thin-wall structures *Struct. Health Monit.* **3** 121–40
[13] Moyo P and Brownjohn J M W 2002 Detection of anomalous structural behaviour using wavelet analysis *Mech. Syst. Signal Process.* **16** 429–45
[14] Chang F K 2002 Introduction to health monitoring: context, problems, solutions *Presentation at the 1st European Pre-workshop on Structural Health Monitoring (Paris, July 2002)*
[15] Anton S R, Inman D J and Park G 2009 Reference-free damage detection using instantaneous baseline measurements *AIAA J.* **47** 1952–64
[16] Badcock R A and Birt E A 2000 The use of 0–3 piezocomposite embedded Lamb wave sensors for detection of damage in advanced fibre composites *Smart Mater. Struct.* **9** 291–7
[17] Lin X and Yuan F G 2005 Experimental study applying a migration technique in structural health monitoring *Struct. Health Monit.—Int. J.* **4** 341–53
[18] Ostachowicz W, Kudela P, Malinowski P and Wandowski T 2009 Damage localisation in plate-like structures based on PZT sensors *Mech. Syst. Signal Process.* **23** 1805–29
[19] Park H W, Sohn H, Law K H and Farrar C R 2007 Time reversal active sensing for health monitoring of a composite plate *J. Sound Vib.* **302** 50–66
[20] Ihn J B and Chang F K 2004 Detection and monitoring of hidden fatigue crack growth using a built-in piezoelectric sensor/actuator network: I. Diagnostics *Smart Mater. Struct.* **13** 609–20
[21] Kundu T, Das S and Jata K V 2009 Health monitoring of a thermal protection system using lamb waves *Struct. Health Monitor.—Int. J.* **8** 29–45
[22] Park S, Yun C-B, Roh Y and Lee J-J 2006 PZT-based active damage detection techniques for steel bridge components *Smart Mater. Struct.* **15** 957–66
[23] Zhao X L, Gao H D, Zhang G F, Ayhan B, Yan F, Kwan C and Rose J L 2007 Active health monitoring of an aircraft wing with embedded piezoelectric sensor/actuator network: I. Defect detection, localization and growth monitoring *Smart Mater. Struct.* **16** 1208–17
[24] Tua P S, Quek S T and Wang Q 2005 Detection of cracks in cylindrical pipes and plates using piezo-actuated Lamb waves *Smart Mater. Struct.* **14** 1325–42
[25] Barke D and Chiu W K 2005 Structural health monitoring in the railway industry: a review *Struct. Health Monitor.* **4** 81–93
[26] Rose J L, Avioli M J and Song W-J 2002 Application and potential of guided wave rail inspection *Insight* **44** 353–8
[27] Wilcox P, Evans M, Pavlakovic B, Alleyne D N, Vine K, Cawley P and Lowe M 2003 Guided wave testing of rail *Insight* **45** 413–20
[28] Rose J L 1999 *Ultrasonic Waves in Solids* (New York: Cambridge University Press)
[29] Su Z and Ye L 2004 Selective generation of Lamb wave modes and their propagation characteristics in defective composite laminates *Proc. Inst. Mech. Eng.* L **218** 95–110
[30] Su Z Q and Ye L 2009 *Identification of Damage Using Lamb Waves: From Fundamentals to Applications* (London: Springer)
[31] Lu Y, Ye L, Su Z Q and Yang C H 2008 Quantitative assessment of through-thickness crack size based on Lamb wave scattering in aluminium plates *NDT&E Int.* **41** 59–68
[32] Walpole R E, Myers R H and Myers S L 1998 *Probability and Statistics for Engineers and Scientists* (Upper Saddle River, NJ: Prentice-Hall)
[33] Ihn J B and Chang F K 2008 Pitch-catch active sensing methods in structural health monitoring for aircraft structures *Struct. Health Monit.—Int. J.* **7** 5–19
[34] Wang C H, Rose J T and Chang F K 2004 A synthetic time-reversal imaging method for structural health monitoring *Smart Mater. Struct.* **13** 415–23
[35] Michaels J E and Michaels T E 2007 Guided wave signal processing and image fusion for *in situ* damage localization in plates *Wave Motion* **44** 482–92
[36] Konstantinidis G, Wilcox P D and Drinkwater B W 2007 An investigation into the temperature stability of a guided wave structural health monitoring system using permanently attached sensors *IEEE Sensors J.* **7** 905–12
[37] Su Z Q, Wang X M, Cheng L, Yu L and Chen Z P 2009 On selection of data fusion schemes for structural damage evaluation *Struct. Health Monit.* **8** 223–41